Review paper

Modeling of Solid-Oxide Fuel Cells

By Vinod M. Janardhanan and Olaf Deutschmann*

Institute for Chemical Technology and Polymer Chemistry, University of Karlsruhe
(TH), Engesserstr 20, D-76131 Karlsruhe, Germany

This article presents a brief review on modeling philosophies of solid-oxide fuel cells
(SOFCs) including an introduction to SOFC components and their functions. While
a plethora of numerical models is available for SOFC modeling and simulation, this
paper focuses on a general overview on mathematical model equations that represent
the physico-chemical processes occurring in SOFCs and their boundary conditions.
Electrochemical model equations, their simplifications, significance, and solution methods
are discussed. Charge transfer chemistry is described in detail from a global as well
as from elementary charge transfer perspective. Principles of heterogeneous reforming
chemistry on conventional nickel cermet anodes, evaluation of rate expressions, and the
implementation of the thermo chemistry into SOFC flow models are described. Results
of numerical simulations are presented for configurations ranging from complex stacks to
simple zero dimensional electrochemical systems.

1. Introduction

Fuel cell is an old concept, dating back to the nineteenth century work of
British scientist Sir William Robert Grove [1]. Grove's experiment in 1839 of
electrolysis of water and his subsequent reasoning of reverse electrolysis to
produce electricity and water resulted in the device which we now refer to
as fuel cell. However, the fuel cell took significant time to mature as a tech-
nology and is still not ready to exploit the niche domestic market. Home
applications in the range of 10 kW are viable only if the system costs can

---

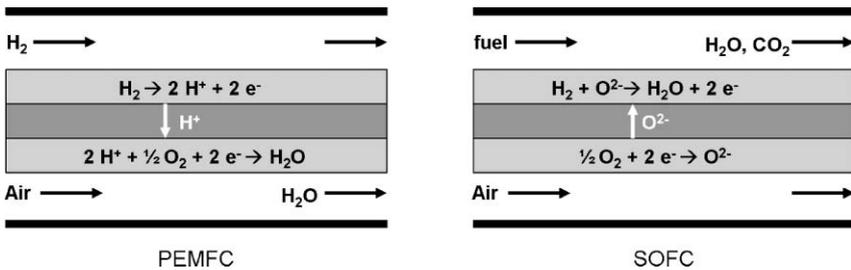 * Corresponding author. E-mail: deutschmann@ict.uni-karlsruhe.de

Fig. 1. Comparison sketch of Proton Exchange Membrane Fuel Cell (PEMFC) and Solid-Oxide Fuel Cell (SOFC).

be brought down to $400/kW. In the early days (1960s), the expenses associated with the cell manufacturing prohibited terrestrial applications and fuel cells were only considered for space applications, for which weight and safety are of major concern. Since that time, fuel cell technology has significantly grown and offers promising routes for inexpensive and clean energy, today. A recent survey of fuel cell activity and commercialization is given by Adamson *et al.* [2].

The well-known and meanwhile fairly mature Proton Exchange Membrane Fuel Cell (PEMFC) applies a proton-conducting polymer electrolyte and precious metals containing electrodes. Due to its low operating temperature of 100 °C, carbon monoxide (CO) poisons the electrodes, hence, the cell needs to be operated with fairly pure hydrogen fuel requiring good pre-reforming and separation of any hydrocarbon containing fuel feedstock. In contrast to the PEMFC, the Solid-Oxide Fuel Cell (SOFC) (Fig. 1) is still under development and applies a ceramic electrolyte, conducting oxygen-ions. SOFCs are completely solid state devices [1] operated at high temperature (500–1000 °C). Hence, CO is not a poison and hydrocarbon containing fuels can in principle be used without upstream fuel processing. This feature of SOFCs definitely is very attractive and opens up a wide range of fuel choices, starting from hydrogen to natural gas, ethanol, and liquid hydrocarbon mixtures. Efficiently running on these fuel systems makes SOFCs a viable candidate for applications such as stationary power generation and auxiliary power units (APUs). Like any other fuel cell system, the SOFC are made up of different components; an overview on SOFC components and materials is given by Weber *et al.* [3].

Although the objective of this article is to line out the principles of SOFC modeling, first we describe the different components of a SOFC unit cell and the various irreversible losses that are encountered during the operation of the cell as a basis for the discussion of modeling principles. Figure 2 (given in Chapter 5) illustrates the components of a planar anode-supported SOFC and the major transport and reaction processes for fuels containing hydrocarbons.

1.1 Anode

The anode typically is a porous structure of ceramic and metal materials (cermets), which are the ionically and electronically conducting phases, respectively. The metallic phase is required for the transport of electrons, which are released at the three phase boundary (TPB) at the anode–electrolyte interface, while the ceramic phase facilitates the transport of oxygen ions. The metallic phase usually is catalytically active for heterogeneous gas-phase reactions. Controlling the composition and micro-structure is critical for the activity of electrodes [4]. Percolating networks of three-phase boundaries formed by the electronic phase, ionic phase, and the gas-phase are important for high electrochemical performance of the cell. The anode of a SOFC in principle should meet a variety of requirements: it should be catalytically active, it should be an electronic conductor, it should exhibit thermal expansion properties matching those of the other components, it should be mechanically stable and should transport the reactants and products to/from the three-phase boundary [5, 6]. Unfortunately none of the existing anode materials meets all of the requirements.

1.1.1 Ni/YSZ anode

The most commonly used anode cermet is nickel/yttria stabilized zirconia (Ni/YSZ). In techniques of the fabrication of NiO/YSZ anodes [7, 8], this layer as fired is a dense material, and most of the porosity results from the reduction process [9]. A three-dimensional reconstruction of the typical state of the art cell with Ni/YSZ anode and its three-phase boundaries are reported in [9].

There are still serious problems for the direct operation of hydrocarbons on Ni/YSZ anodes due to the coking propensity of Ni for hydrocarbons [10]. Furthermore, Ni/YSZ anodes are found to deteriorate over time and are less tolerant to sulfur and suffer from volume instability due to poor redox cycling [11, 12]. Therefore a number of researchers have tried different anodic materials and barrier layers, which are resistant to coke formation during direct operation on hydrocarbons [13, 14].

1.1.2 Ceria based anode

Ceria based anodes, *e.g.* yttria or samaria doped ceria (YDC, SDC), are good choices for direct operation on hydrocarbons [15, 16], because they are widely recognized for their ability to suppress coking, which permits the utilization of methane rich fuels at low steam to carbon ratio. Both doped and non doped ceria display mixed ionic and electronic conduction at low oxygen partial pressure. The main draw back of the ceria based anode is the lattice expansion at low oxygen partial pressures. This can lead to cracks at the electrode–electrolyte interface and the subsequent delamination of the electrode from the electrolyte interface, especially with YSZ electrolyte [17].

However, doping with cations of gadolinium (Gd^{3+}), samarium (Sm^{3+}), or yttrium (Y^{3+}) can significantly reduce the dimensional contraction during reduction.

1.1.3 Perovskite anodes

The replacement of Ni/YSZ by Ni free materials with similar electro-catalytic properties is in the focus of many research groups in order to increase the durability of the anode. Among many different materials, perovskite-type ceramics have received special attention. The perovskite structure has the generic formula ABO_3, in which the A sites are occupied by large cations such as La, Sr, Ca, and Pb at the corners of the cubic unit cell and the B sites at the cube centers are occupied by smaller cations such as Ti, Cr, Ni, Fe, Co, and Zr. These smaller cations are surrounded by six oxygen ions in an octahedral coordination [11]. Varying levels of electronic and ionic conduction can be achieved by different combinations of cations. A very useful property of perovskites is their mixed ionic and electronic conductivity, which can result in increased three-phase boundary length and hence enhanced electro oxidation. Tao *et al.* [12] reported a Ni free perovskite anode ($La_{0.75}Sr_{0.25}Cr_{0.5}Mn_{0.5}O_3$) exhibiting an electrochemical performance comparable to conventional Ni/YSZ. Furthermore, this perovskite was found to be more tolerant towards carbon deposition. However, a variety of perovskites such as $La_{0.6}Sr_{0.4}Co_{0.2}Fe_{0.8}O_3$ and $LaNi_{1-x}M_xO_3$ (M: Ti, V, Nb, Mo, W) are not stable in reducing atmosphere due to the generation of oxygen vacancies [17].

1.2 Cathode

At the SOFC cathode, oxygen is reduced supplying the ions to the electrolyte. The cathode should transport air from the cathode channel towards the three-phase boundary. In most cases, the cathodes consist of perovskite materials like strontium-doped lanthanum manganite (LSM) [15, 18] or $La_{0.84}Sr_{0.16}Co_{0.3}Fe_{0.7}O_3$ (LSCF) [19], which are efficient catalysts for the dissociation of oxygen molecules [11]. In general, the activation loss at the cathode by far exceeds that of the anode and frequently is the limiting factor for the performance of the SOFC [20, 21]. This loss is caused by the kinetics of oxygen reduction, hence, any material that can efficiently catalyze the formation of O^{2-} ions results in a reduced overpotential loss. For instance, the application of a multilayer LSM cathode has been reported to decrease the overpotential losses significantly [22]. In general, decreasing the grain size while maintaining high porosity is beneficial for high current density. Therefore multi-layered cathodes with larger grains on the outer layer and smaller grains on the inner layer can significantly increase the performance [23, 24].

The performance of the cathode is affected by several factors such as materials composition, materials processing, sintering conditions, density, surface

morphology, and resistivity [21]. Moreover, the influence of these parameters on cathode performance is not static; rather it changes and evolves during fuel cell operation [25]. The cathode performance may adversely be affected by other SOFC components, for instance by interconnects made out of Cr alloys during high temperature operation [20, 26].

1.3 Electrolyte

The electrolyte of a SOFC sandwiched between the anode and the cathode is a ceramic material that is impervious to gas transport. Any gas transport would lead to thermal oxidation of the fuel releasing heat, which otherwise would have contributed to the release of electrical energy. In general, the electrolyte should be a very good ionic conductor to facilitate the transport of oxygen ions formed at the cathode–electrolyte interface towards the electrolyte–anode interface. Furthermore, the electrolyte should have no electronic conductivity, otherwise electrons will diffuse to the cathode without passing the external load. The electrolyte should also be stable in both oxidizing and reducing atmospheres. Though electrolytes can serve as structural support for SOFCs, in that case electrolytes of thickness of $\sim 150\,\mu m$ are used [3], more and more attention is paid to anode-supported cells. Hence, thin film electrolytes ($\sim 10\,\mu m$) are in the focus of electrolyte research [20]. The use of 10–20 μm thin electrolytes decreases the losses due to Ohmic resistance [27].

Due to its excellent stability in both oxidizing and reducing atmospheres, YSZ is the most common electrolyte material. Electrolyte-supported cells with YSZ as electrolyte material cause problems during high temperature operation [4]. Therefore, other O^{2-}-conducting materials such as $LaGaO_3$ were proposed for electrolyte supported cells. Ceria based electrolytes such as Gd_2O_3 doped CeO_2 (GDC) have higher ionic conductivity than YSZ and are preferred for intermediate temperature (700–800 °C) applications [19]. Scandia doped zirconia (SDZ) and ceria based materials were proposed for operating temperatures below 700 °C and below 550 °C, respectively [28].

1.4 Interconnect

The interconnect serves as electrical contact between the anode of one individual cell to the cathode of the neighboring cell and as physical barrier for the protection of the cathode/anode material of one individual cell from the reducing/oxidizing environment of the neighboring fuel/air channel [29]. Therefore, the interconnect materials must be stable in oxidizing and reducing environments [30]. In certain stack constructions, the interconnect also serves as a structural support material [31]. Interconnects can significantly contribute to the costs of the stack depending on the operating temperature [20]. In high temperature SOFCs, the interconnect is made out of ceramic materials such as lanthanum chromate or sophisticated refractory alloy. The commonly used interconnect materials are doped $LaCrO_3$ based materials [12]

and high-temperature oxidation resistant alloys. Compared to ceramic inter-connects metallic interconnects offer high electrical conductivity and are less expensive. However, the electronic conductivity of metallic interconnects also depends on the dopants and the doping level [32]. The two most common dopants added to lanthanum chromate are strontium and calcium. At high operating temperatures the metallic interconnects such as Fe-based or Ni-based alloys are easily oxidized [33]. The contact resistance of an oxidized metallic interconnect is usually characterized in terms of area specific resistance (ASR) and the generally accepted value is less than $0.1\,\Omega\,cm^2$ [27]. Combined with thin film electrolytes metallic interconnects are considered as highly practical in low temperature applications.

2. Fuels and fuel processing

2.1 Fuels

Most solid oxide fuel cells still use hydrogen as fuel, and fuel cells which can use other fuels typically work best with hydrogen [34]. Today, however, running SOFCs on direct hydrocarbons is of great interest [35–37]. Natural gas, due to its widespread availability and distribution infrastructure, is an ideal choice for stationary SOFC applications [34, 38]. Propane and butane are preferred for portable applications [39] due to their high energy density. Furthermore, they are readily available, inexpensive, and the lowest molecular weight hydrocarbons that can be easily used as liquids [34]. Methanol and ethanol have also been considered for portable fuel-cell applications. Though there are reports on the operation of SOFCs with ethane, propane [40, 41], butane [14, 39], and octane [37], these are limited to a laboratory environment. A list of fuels that can be used in SOFCs is given in [42].

The choice of the appropriate fuel also strongly depends on the operating temperature of the cell. Natural gas and higher hydrocarbons can be efficiently internally reformed in SOFCs operating above 600 °C. For operating temperatures as low as 500 °C oxygenates such as methanol or ethanol are considered the most suitable fuels due to the low temperature required for reforming these fuels [43].

Running SOFCs on these alternate fuels calls for a good understanding of the thermo chemistry in the anode, because the hydrocarbons easily undergo cracking and partial oxidation.

2.2 Fuel processing

Today, existing installations of SOFC plants do not feed hydrocarbon fuels, mainly due to electrode stability issues. Instead, hydrocarbons are pre-reformed prior to feeding to the fuel cell stack. Furthermore, SOFC anodes are

not tolerant to sulfur content in natural gas. Therefore all existing installations require some amount of fuel processing at least [34, 44].

The high temperature, at which a SOFC is operated, prevents poisoning of the anode by adsorption of CO. Therefore, SOFCs can principally use hydrocarbons as fuel. The electrochemical activity of various chemical species is still a debatable topic. However there is no doubt on the high electrochemical activity of H_2 and CO [45–47]. Therefore, any fuel used in SOFC shall finally be converted into H_2 and/or CO for enabling charge transfer. The fuel processing can be achieved either internaly or externaly [48]. An external reformer results in additional costs of the overall system and hence internal reforming is an attractive option. Internal reforming can be carried out either in a separate fuel reformer integrated within the stack (indirect internal reforming), or directly on the fuel cell anode (direct internal reforming) [42]. Indirect internal reforming increases the system efficiency by recuperating the waste heat from the stack into the fuel supply.

The direct internal reforming of hydrocarbons can eliminate the need of a fuel reformer and the extra cooling air which would otherwise be required in an SOFC running on hydrogen. Thus the direct internal reforming may result in an increased overall efficiency [15]. However, direct internal reforming of hydrocarbons without upstream reforming is challenging due to the possibility of anode fouling [49] that is the formation of carbonaceous overlayers (coke). Issues related to coking have been recently studied by many groups [10, 13, 50].

Since the application of alternate fuels calls for advanced anode materials, considerable efforts aim at their improved thermo-catalytic, structural, and electrical properties [14, 51]. A noted review mentions that, *"Although cost is clearly the most important barrier to the widespread SOFC implementation, perhaps the most important technical barriers currently being addressed relate to the electrodes, particularly the fuel electrode or anode"* [34].

3. Modeling electrochemistry

Connected to an external load, the potential difference across the electrodes of a fuel cell drives the electrons through the external circuit. However, the detailed processes in the electrochemical system are quite complex in nature. Even though many studies have been devoted to the charge transfer at the interfaces formed by the electrodes and electrolyte, it still remains one of the least understood aspects of electrochemistry.

The operation of the cell is associated with various irreversibilities and leads to various potential losses. In the case of electrodes, the total resistance comprises of the internal resistance, contact resistance, activation polarization resistance, and concentration polarization resistance. Internal resistance refers to the resistance for electron transport, which is usually determined by the

electronic conductivity and the thickness of the electrode structure. Contact resistance refers to the poor contact between the electrode and the electrolyte structure. All resistive losses are functions of the local current density. The overpotential losses can be minimized by an appropriate choice of electrode material and the control of the micro-structural properties during the manufacturing process.

3.1 Activation overpotential

The activation overpotential is associated with the charge transfer process and can be considered as the slowness of the electrochemical charge transfer reaction taking place at the three-phase boundary. The maximum voltage that can be harnessed from the cell under reversible conditions is the open circuit voltage/potential (OCV). However during operation, the cell has to overcome the irreversibilities associated with the processes. Therefore a fraction of the open circuit potential is utilized to drive the charge transfer reaction taking place at the three-phase boundaries. This is known as the activation overpotential. The higher the resistance for charge transfer reaction, the higher will be the activation overpotential.

3.1.1 Butler–Volmer equation

The Butler–Volmer equation relates the activation overpotential, η_{act}, to the current density, i:

$$i = i_0 \left[\exp\left(\alpha_a \frac{n_e F \eta_{act}}{RT} \right) - \exp\left(-\alpha_c \frac{n_e F \eta_{act}}{RT} \right) \right]. \tag{1}$$

However, the complete understanding and definitions of activation overpotential and the asymmetry factors, α_a and α_c, are potentially confusing. During anodic charge transfer the electrons are released at the anode–electrolyte interface and move towards the cathode through the external circuit. The electric current by convention flows in the opposite direction. The electrons (negatively charged) always flow towards the positive terminal, which is the cathode. In order to drive the electrons to the region of lower potential, energy needs to be supplied. Therefore, energy has to be spent to drive the electrons from the electrolyte to the anode (in the case of anode charge transfer). The amount of energy required to drive the electrons depends on the relative potential difference between the anode and the electrolyte. The electric potential of the anode is always lower than that of the electrolyte. Therefore the forward reaction can be facilitated by increasing the anode potential, i.e. making it less negative. At equilibrium anode electrical potential difference, $E_a^{eq} = \phi_a^{eq} - \phi_{e,a}^{eq}$, the reaction proceeds in the anodic and cathodic direction at equal and opposite rates. The activation overpotential, η_{act}, is the potential difference exceeding the equilibrium potential difference between the anode and the electrolyte. The electric

potential difference between the anode and electrolyte is $E_a = \phi_a - \phi_e$, and the activation overpotential is $\eta_{act} = E_a - E_a^{eq}$.

The exchange current density, i_0 in Eq. (1), is usually expressed as a function of species concentrations, $[X]_k$ [52]:

$$i_0 = i_0^0 \prod_{k=1}^{K} [X]_k^{\gamma_k} . \tag{2}$$

i_0^0 can further be expressed as function of temperature in the Arrhenius form [53]:

$$i_0^0 = A \exp\left(\frac{-E_a}{RT}\right). \tag{3}$$

Although this form of exchange current density provides flexibility in the model, it is quite difficult to determine the reaction orders γ_k and is far from a general description of elementary charge transfer steps. Furthermore, the reaction orders estimated from exchange current density considerably differ from those derived from elementary step kinetics.

In general, the charge transfer coefficients, α_a and α_c, follow the relation $\alpha_a + \alpha_c = 1$. If the charge transfer coefficients are assumed to be 0.5 then the Butler–Volmer equation (Eq. (1)) can be inverted to evaluate the activation overpotential for a given current density as

$$\eta_a = \frac{2RT}{n_e F} \sinh^{-1}\left(\frac{i}{2i_{0a}}\right) \tag{4}$$

and

$$\eta_c = \frac{2RT}{n_e F} \sinh^{-1}\left(\frac{i}{2i_{0c}}\right) . \tag{5}$$

Here, i_{0a} and i_{0c} are the exchange current densities for the anode and cathode charge transfers, respectively [54].

3.1.2 Limiting cases of Butler–Volmer equation

Two limiting cases exist for Eq. (1). At very high activation overpotential the first exponent in Eq. (1) turns out to be much greater than the second exponent and, hence, the second one can be neglected leading to

$$\eta_{act} = \left(\frac{RT}{\alpha_a n_e F}\right) \ln i - \left(\frac{RT}{\alpha_a n_e F}\right) \ln i_0 , \tag{6}$$

which is the well known Tafel equation.

For very low activation overpotentials ($\eta_{act} \ll 1$), the argument $\alpha_a n_e F / RT$ becomes much less than unity and the exponent can be expanded in terms

of Taylor series. Neglecting the higher order terms lead to the linear current–potential relation

$$\eta_{\text{act}} = i \frac{RT}{n_e F i_0} . \tag{7}$$

Though the limiting cases of Butler–Volmer equations are easy to use, one should be careful about the range of activation overpotential, in which these equations are valid. Chan *et al.* [54] reported the lower limit of activation overpotential for which the Tafel equation can be used as $\eta_{\text{act}} > 0.28$ V, and the upper limit for the linear current–potential relation as $\eta_{\text{act}} < 0.1$ V.

3.2 Ohmic overpotential

The major contribution to the Ohmic overpotential is the ionic resistance of the electrolyte material. In the state of the art anode supported cell the Ohmic losses are minimal due to the use of thin film electrolytes which are usually 5–10 μm thick. The Ohmic losses can be further reduced by operating the cell at high temperatures. However the high temperature operation is not preferred due to the detrimental effects on the cell life time and the costs of ceramic materials required for high temperature operation [55].

The electrodes also contribute to Ohmic overpotential due to internal resistance. In the case of mixed electronically and ionically conducting electrodes such as perovskites both ionic and electronic conductivity determine the total internal resistance. The electronic properties strongly depend on composition and micro-structure. For Ni/YSZ cermet the electronic conductivity changes with Ni content. The percolation theory predicts an S-shaped curve for the cermet conductivity as a function of Ni content. The percolation threshold (the Ni content at which the conductivity starts to increase) is found to be approximately 30% depending on porosity, pore size, and particle size distribution [17].

The Ohmic overpotential can be expressed as a function of local current density, i, as

$$\eta_{\text{ohm}} = i R_{\text{tot}} , \tag{8}$$

where R_{tot} is the total cell resistance consisting of the contributions of individual cell components:

$$R_{\text{tot}} = \rho_e l_e + \rho_a l_a + \rho_c l_c + R_{\text{contact}} . \tag{9}$$

In the above equation ρ_e, ρ_a, and ρ_c are the specific electrical resistances of electrolyte, anode, and cathode, respectively; l_e, l_a, and l_c are the thickness of electrolyte, anode, and cathode, respectively, and R_{contact} is any contact resistance present in the system.

The contribution of the electrolyte to Ohmic resistance can be expressed as

$$\rho_e = \frac{1}{\sigma_e} . \tag{10}$$

Here, σ_e is the ionic conductivity of the electrolyte strongly depending on temperature; generally it is expressed as

$$\sigma_e = \frac{\sigma_0}{T} \exp(-E_e/RT) , \tag{11}$$

where E_e is the activation energy for ion transport.

The total resistance on the anode/cathode side comprises of internal resistance towards the transport of electrons (ions as well in the case of mixed ionic electronic conductors) and contact resistance, that is the resistance caused by the poor adherence between the anode and the electrolyte. The magnitudes of all these resistances depend on the particular material and microstructure.

3.3 Concentration overpotential

The concentration overpotential arises from the transport limitations within the porous electrode structure. The maximum cell potential depends on the partial pressures of electrochemically active reactants and products of the charge transfer reaction at the TPBs as described by the Nernst equation (Eq. (32)). However, the concentrations of chemical species at the TPB differ from those in the fuel and oxidizer channels due to transport processes. The reactants have higher concentrations in the flow channels than at the electrode–electrolyte interfaces, where the products have higher concentrations.

The concentration overpotential strongly depends on the electrode microstructure. A high tortuosity and low porosity can lead to high concentration overpotentials.

Based on the assumption of equi-molar counter diffusion and H_2 as fuel, Chan *et al.* [54] derived an analytical expression for the concentration overpotential:

$$\eta_{\text{conc,a}} = -\frac{RT}{2F} \ln \left[\frac{(1 - (RT/2F)(l_a/D_e p_{H_2}^I)i}{(1 + (RT/2F)(l_a/D_e p_{H_2O}^I)i} \right] , \tag{12}$$

$$\eta_{\text{conc,c}} = -\frac{RT}{4F} \ln \left[\frac{(p_c/\delta_{O_2}) - ((p_c/\delta_{O_2}) - p_{O_2}^I)}{p_{O_2}^I} \right.$$
$$\left. \times \frac{\exp\left[(RT/4F)(\delta_{O_2} l_c/D_e p_c)i\right]}{p_{O_2}^I} \right] . \tag{13}$$

Here, D_e is the effective diffusion coefficient, p_i^I are the partial pressures of the chemical species at the inlet conditions, l_a and l_c are thickness of anode and cathode, respectively. The concentration overpotential can also be expressed as a function of limiting current density,

$$\eta_{conc} = \frac{RT}{n_e F} \ln\left(1 - \frac{i}{i_l}\right), \tag{14}$$

where i_l is the limiting current density [56].

   With hydrocarbons as fuel, the scenario becomes more complicated due to multi-component transport. The diffusive transport within the pore structure is controlled by both, Knudsen and molecular diffusion. With hydrocarbon fuels, numerous chemical reactions proceed in the porous anode and the concentration overpotential has to be evaluated numerically. An appropriate model approach is the solution of this porous media transport–reaction problem by the Dusty Gas Model (DGM) discussed below. However, many studies adhere to the simple analytical expression derived for H_2 even for the case of hydrocarbons to reduce the numerical complexity [57].

3.4 Charge transfer

In general, the charge transfer chemistry proceeds through electrochemically active species such as H_2 and CO. Hydrogen oxidation kinetics usually dominates over CO oxidation [58]. As mentioned earlier the understanding of the kinetics, reaction pathways, and the rate limiting steps remains a complex and challenging task in SOFC research. Even for the simplest case of hydrogen oxidation a large number of reaction steps occur at the TPB, and several possible reaction pathways were proposed [47, 59–61]; a discussion on this is given in [5]. Recently, there has been some consensus regarding the reaction pathway for hydrogen oxidation on Ni/YSZ anodes [62, 63]. In general, the postulated reaction pathways can be grouped into two major categories namely the oxygen spillover and the hydrogen spillover mechanism. Bessler *et al.* [62, 63] demonstrated draw backs of oxygen spillover mechanism and concluded that the hydrogen spillover is the likely reaction pathway. They also asserted that the rate limiting charge transfer step is the hydrogen spillover from the Ni surface to a hydroxyl group on the YSZ surface.

3.4.1 Hydrogen oxidation

 Hydrogen oxidation is the most studied charge transfer reaction in solid-oxide electrochemical systems [5, 46, 47, 58–61, 64]. The global hydrogen oxidation reaction,

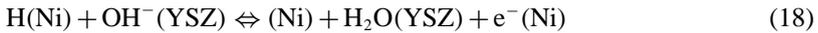$$H_2 + O^{2-} \Leftrightarrow H_2O + 2e^-, \tag{15}$$

proceeds *via* multi-step adsorption, desorption, and reaction steps. A possible sequence of reactions is listed below [65]:

1) Adsorption/desorption of H_2 on Ni surface

$$H_2 + (Ni) + (Ni) \Leftrightarrow H(Ni) + H(Ni) \tag{16}$$

2) Charge transfer at TPB

$$H(Ni) + O^{2-}(YSZ) \Leftrightarrow (Ni) + OH^-(YSZ) + e^-(Ni) \tag{17}$$

$$H(Ni) + OH^-(YSZ) \Leftrightarrow (Ni) + H_2O(YSZ) + e^-(Ni) \tag{18}$$

3) Adsorption/desorption of H_2O on YSZ surface

$$H_2O(YSZ) \Leftrightarrow H_2O + (YSZ) \tag{19}$$

4) Oxygen ion transfer between the bulk and surface YSZ

$$V_o^{\bullet\bullet}(YSZ) + O^{2-}(YSZ) \Leftrightarrow (YSZ) + O_o^{\times}(YSZ) \,. \tag{20}$$

The symbols in the brackets stand for the corresponding surface, to which the particular species is attached; for example, H(Ni) stands for a hydrogen atom attached to the Ni surface, and (Ni) represents an uncovered Ni surface site. $O_o^{\times}(YSZ)$ is a lattice oxygen, and $V^{\bullet\bullet}(YSZ)$ is an oxygen vacancy. Although, in principle, any of these reactions can be rate limiting, Zhu *et al.* [65] assumed reaction 18 to be rate limiting and the other reactions to be in partial equilibrium; later this idea was supported by Bessler *et al.* [63]. Based on these assumptions, the phenomenological Butler–Volmer equation takes the form:

$$i = i_0 \left[\exp\left(\frac{(1+\beta_a)F\eta_a}{RT} \right) \exp\left(-\frac{\beta_c F\eta_a}{RT} \right) \right]. \tag{21}$$

Here, $\eta_a = E_a - E_a^{eq}$ is the anodic activation overpotential, and β is the charge transfer coefficient or the asymmetry factor. For single step electron transfer reactions the charge transfer coefficients always obey the condition $\beta_a + \beta_c = 1$. The exchange current density, i_0, depends on temperature and chemical composition [53, 65]:

$$i_0 = k_{H_2} \exp\left(-\frac{E_{H_2}}{RT} \right) \frac{\left(p_{H_2}/p_{H_2}^* \right)^{1/4} (p_{H_2O})^{3/4}}{1 + \left(p_{H_2}/p_{H_2}^* \right)^{1/2}} \,. \tag{22}$$

The complex reaction order dependence of exchange current density in H_2 and H_2O are quite different from the ones used for global charge transfer chemistry [66]. The parameter $p_{H_2}^*$ is given as [65]:

$$p_{H_2}^* = \frac{A_{H_2} \Gamma^2 \sqrt{2\pi RTW_{H_2}}}{\gamma_0} \exp\left(-\frac{E_{H_2}^{des}}{RT} \right). \tag{23}$$

Here, Γ is the surface site density, a value of 2.6×10^{-9} mol/cm^2 was chosen for Ni. The pre-exponential factor and the activation energy, $A_{H_2} = 5.59 \times 10^{19}$ cm^2 s^{-1} mol^{-1} and $E_{H_2}^{des} = 88.12$ kJ mol^{-1}, respectively, are determined by fitting the model to experimental data [53].

3.4.2 Oxygen reduction

As in the case of H$_2$ oxidation, the oxygen reduction on the cathode also proceeds in a multi-step mechanism. The adsorption of O$_2$ on the cathode surface is followed by the dissociation into two O atoms and the surface diffusion to the three-phase boundary region. The oxygen atoms take part in a number of electron transfer steps reducing O to O^{2-}. However, there is no conclusive identification of the rate limiting step. The overall oxygen reduction reaction and the incorporation of the ions into the electrolyte can be written in Kröger–Vink notation as

$$\frac{1}{2}O_2 + V_o^{\bullet\bullet}(el) + 2e^-(c) \Leftrightarrow O_o^\times(el). \tag{24}$$

This global reaction can be split into a number of steps, for instance:
1) Adsorption/desorption of oxygen

$$O_2 + (c) + (c) \Leftrightarrow O(c) + O(c) \tag{25}$$

2) Surface diffusion to three-phase boundary region

$$O(c) \Leftrightarrow O(TPB) \tag{26}$$

3) Formation of O^{2-} ions and the subsequent incorporation into the electrolyte

$$O(TPB) + V_o^{\bullet\bullet}(el) \Leftrightarrow O_o^\times(el) + (TPB) \tag{27}$$
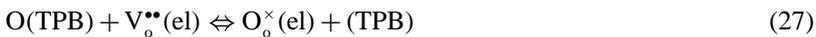
Assuming the charge transfer step, Eq. (27), to be rate limiting, Zhu *et al.* [65] derived an expressions for the Butler–Volmer equation:

$$i = i_0 \left[\exp\left(\frac{\beta_a F \eta_c}{RT}\right) - \exp\left(-\frac{\beta_c F \eta_c}{RT}\right) \right], \tag{28}$$

with the exchange current density as

$$i_0 = k_{O_2} \exp\left(-\frac{E_{O_2}}{RT}\right) \frac{\left(p_{O_2}/p_{O_2}^*\right)^{1/4}}{1 + \left(p_{O_2}/p_{O_2}^*\right)^{1/2}}, \tag{29}$$

where $p_{O_2}^*$ is given by

$$p_{O_2}^* = A_{O_2} \exp\left(-\frac{E_{O_2}^{des}}{RT}\right). \tag{30}$$

Here, $A_{O_2} = 4.9 \times 10^8$ atm and $E_{O_2} = 200$ kJ/mol. k_{O_2} and E_{O_2} can be deduced by adapting the model to experimental data [53]. The activation energy of the oxygen reduction reaction on LSM-YSZ cathodes is reported to range from 100 to 200 kJ/mol [18].

3.5 Nernst equation and cell potential

The cell potential is the operating potential of the cell, resulting from the collected differences in the electric potential between the various phases in the cell [67]. The operating cell potential depends on the overpotential losses and can be written as a function of local current density i:

$$E_{cell} = E_{rev} - \eta_a(i) - |\eta_c(i)| - \eta_{ohm}(i) - \eta_{conc}(i) \,, \tag{31}$$

where η_a and η_c are the activation losses at the anode and cathode side respectively, η_{ohm} is the Ohmic overpotential, and η_{conc} is the concentration overpotential. If the electrode models treat flow through porous media using appropriate transport equations, then concentration overpotentials do not need to be explicitly considered and vanish in Eq. (31). For the case of hydrogen oxidation E_{rev} in Eq. (31) is given by the well known Nernst equation:

$$E_{rev} = E^0 + \frac{RT}{2F} \ln \left(\frac{p_{H_2,a} \, p_{O_2,c}^{1/2}}{p_{H_2O,a}} \right) \,. \tag{32}$$

In the above equation E^0 is the electro-motoric force (EMF) at standard pressure. Equation (32) can be substituted back in Eq. (31). The Ohmic loss in Eq. (31) was already defined in Eq. (8) as $\eta_{ohm} = R_{tot}i$, where R_{tot} is the total resistance. In modern cells, however, the resistance contributed by the anode and cathode materials are negligible compared to the electrolyte resistance.

The Nernst potential, E_{rev}, also called open circuit voltage (OCV), is the maximum possible potential that can be derived from a cell operating reversibly. Therefore, the Nernst potential is also known as the reversible potential. Consequently, the actual potential is always lower than the Nernst potential during the operation of the cell due to the irreversibilities.

3.6 Solution procedure for electrochemical equation system

A system of non-linear, coupled equations is formed by Eqs. (21), (28), and (31) that can either be solved for the local current density, i, by fixing the operating cell potential, E_{cell}, or alternatively for the cell potential by fixing the average current density. Assuming the cell potential as the fixed parameter, the residual form for the solution variables can be written as

$$F(\Phi) = 0 \,, \tag{33}$$

where the vector Φ is ordered as

$$\Phi = [i, \eta_a, \eta_c].\tag{34}$$

However, this solution requires iterative methods, for instance a Newton's algorithm.

4. Modeling heterogeneous chemistry

Ni/YSZ is the most commonly used anode material in today's existing installations. Although perovskite materials are drawing much attention, studies reported on these materials are limited to laboratory environment. For any fuel other than hydrogen, catalytic reactions are likely to occur in the anode structure leading to a complex chemical composition of the reactants at the TPB. The products such as H_2O, CO, and CO_2 formed at the TPB will actively take part in the catalytic chemistry. For the application of hydrocarbon fuels, the understanding of the catalytic kinetics is vital for precise prediction of fuel utilization and performance of SOFCs. The use of hydrocarbons may additionally require to consider potential homogeneous reactions in the gas phase [68], which will not be discussed here.

So far, most studies on direct internal reforming of hydrocarbons in SOFC anodes were devoted to methane as hydrocarbon and Ni containing anode structures under conditions being not favorable for homogeneous gas-phase chemistry. Dicks *et al.* [69] studied the intrinsic kinetics of CH_4 steam reforming over Ni/zirconia anodes. They found the reaction to be first order in CH_4 and the reaction orders in H_2 and H_2O to depend either on temperature or the partial pressures of other species. Furthermore, their non-linear Arrhenius plots implied a varying activation energy (118–294 kJ/mol), which significantly differs from deuterium exchange studies of CH_4 over nickel (100–135 kJ/mol). Assuming Langmuir adsorption isotherms and following the mechanistic steps described by Boudart [70] and others, Dicks *et al.* [69] described the rate as

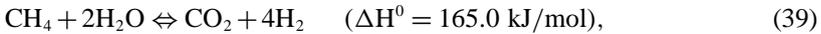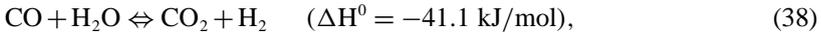$$\dot{s} = \frac{k(T)p_{CH_4}}{\left(1 + K_H(T)p_{H_2}^{1/2} + K_S(T)p_{H_2O}/p_{H_2}\right)^n},\tag{35}$$

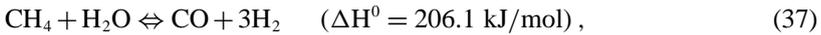with $k(T)$ as rate constant described by

$$k = k_0 \exp\left(\frac{-E_a}{RT}\right).\tag{36}$$

The n in Eq. (35) is the number of surface sites required for CH_4 adsorption, and K_H and K_S are the equilibrium constants for H_2 and H_2O adsorption, respectively. However, the kinetic parameter fit using their measured activation energies led to a physically unrealistic parameter estimation. Therefore

the fits were carried out using the activation energy of the deuterium exchange study. Interestingly their rate expression vanishes at zero H_2 concentration.

Another interesting study dealing with intrinsic kinetics of steam reforming of methane on $Ni/MgAl_2O_4$ is reported by Xu and Froment [71]. They found that the catalyst deactivation rate increase with increasing pressure, temperature, and steam to methane molar ratio and identified two competitive reaction schemes for the formation of CO and CO_2. The first scheme contains the parallel formation of CO and CO_2 from CH_4 and the radicals coming from adsorbed CH_4, while the second scheme contains the parallel formation of CO and CO_2 from adsorbed CHO species. Their rate expressions derived for three global rate determining steps (Eqs. (37)–(39))

$$CH_4 + H_2O \Leftrightarrow CO + 3H_2 \quad (\Delta H^0 = 206.1 \text{ kJ/mol}), \tag{37}$$

$$CO + H_2O \Leftrightarrow CO_2 + H_2 \quad (\Delta H^0 = -41.1 \text{ kJ/mol}), \tag{38}$$

$$CH_4 + 2H_2O \Leftrightarrow CO_2 + 4H_2 \quad (\Delta H^0 = 165.0 \text{ kJ/mol}), \tag{39}$$

are

$$r_{37} = \frac{k_{37}}{p_{H_2}^{2.5}} \left(p_{CH_4} p_{H_2O} - \frac{p_{H_2}^3 p_{CO}}{K_{37}} \right) \Big/ (\text{DEN})^2, \tag{40}$$

$$r_{38} = \frac{k_{38}}{p_{H_2}} \left(p_{CO} p_{H_2O} - \frac{p_{H_2} p_{CO_2}}{K_{38}} \right) \Big/ (\text{DEN})^2, \tag{41}$$

$$r_{39} = \frac{k_{39}}{p_{H_2}^{3.5}} \left(p_{CH_4} p_{H_2O}^2 - \frac{p_{H_2}^4 p_{CO_2}}{K_{39}} \right) \Big/ (\text{DEN})^2, \tag{42}$$

$$\text{DEN} = 1 + K_{CO} p_{CO} + K_{H_2} p_{H_2} + K_{CH_4} p_{CH_4} + K_{H_2O} p_{H_2O}/p_{H_2}.$$

Here, the rate constants, k_i, are expressed in terms of a reference temperature, T_r, as

$$k_i = k_{i,T_r} \exp\left[-\frac{E_i}{R} \left(\frac{1}{T} - \frac{1}{T_r} \right) \right] \quad i = 37, 38, 39, \tag{43}$$

and the adsorption coefficients are expressed as

$$K_j = K_{j,T_r} \exp\left[-\frac{\Delta H_j}{R} \left(\frac{1}{T} - \frac{1}{T_r} \right) \right] \quad j = CO, H_2, CH_4, H_2O. \tag{44}$$

Xu and Froment [71] found the activation energy for the reactions (37, 38, and 39) to be 240.1, 67.13, and 243.9 kJ/mol, respectively.

Ahmed and Foger [72] derived kinetic data for steam reforming under conditions which are economically attractive for fuel cell applications. They assumed the rate equation to be

$$-r_{CH_4} = k p_{CH_4}^{\alpha} p_{H_2O}^{\beta} \exp\left(\frac{-E_a}{RT}\right). \tag{45}$$

The parameters α and β depend on the anode composition and were reported to be 0.85 ± 0.05 and -0.35 ± 0.04, respectively, for typical Ni/ZrO_2 anodes. An activation energy of $95 \pm 2\,kJ/mol$ was given, which significantly differs from the activation energy reported in [69].

Recently, Hecht *et al.* [73] reported a multi-step reaction mechanism for steam reforming of CH_4 on Ni at $800\,°C$. The mechanism predicted steam as well as dry reforming under SOFC operating condition in a Ni/YSZ anode structure, although the mechanism was originally developed on the basis of experiments using monolithic Ni/Al_2O_3 catalysts. The mechanism covers a variety of global aspects of the chemical system such as steam reforming, water-gas shift, reverse water-gas shift, dry reforming, and the Boudouard reaction but does not include Ni oxidation and multilayer carbon deposits on the Ni catalyst. Later, the mechanism was extended to a wider range of temperature conditions [53]. This mechanism consists of 42 reactions among 6 gas-phase species and 12 surface adsorbed species. Most of the reaction rates of the mechanism are expressed in Arrhenius form and some include the dependence of the rate constants on surface coverage with adsorbed species,

$$k_i = A_i T^{\beta_i} \exp\left(-\frac{E_{ai}}{RT}\right) \prod_{k=1}^{K_s} \theta_k^{\mu_{ki}} \exp\left(-\frac{\epsilon_{ki}\theta_k}{RT}\right), \tag{46}$$

where k_i is the rate constant for the reaction i, μ_{ki} and ϵ_{ki} are parameters modeling the coverage dependence of the rate constants and θ_k is the surface coverage of species k. The molar production rate of species k due to catalytic reactions is then given by

$$\dot{s}_k = \sum_{i=1}^{K_r} \nu_{ki} k_i \prod_{k=1}^{K_g+K_s} [X]_k^{\nu'_{ki}}, \tag{47}$$

where K_r is the number of reactions, K_g and K_s are the number of gas-phase and surface species, respectively. ν_{ki} is the difference in stoichiometric coefficients of products and reactants, ν'_{ki} are the stoichiometric coefficients of reactants, and $[X]_k$ is the concentration of the chemical species k. The complete reaction mechanism is listed in Table 1.

Table 1. Heterogeneous reaction mechanism for reforming of CH_4 on Ni.

	Reaction	A^* (cm, mol, s)	β	E_a^* (kJ mol^{-1})
1.	$H_2 + NI(s) + NI(s) \rightarrow H(s) + H(s)$	$1.000 \times 10^{-02\dagger}$	0.0	0.00
2.	$O_2 + NI(s) + NI(s) \rightarrow O(s) + O(s)$	$1.000 \times 10^{-02\dagger}$	0.0	0.00
3.	$CH_4 + NI(s) \rightarrow CH_4(s)$	$8.000 \times 10^{-03\dagger}$	0.0	0.00
4.	$H_2O + NI(s) \rightarrow H_2O(s)$	$1.000 \times 10^{-01\dagger}$	0.0	0.00
5.	$CO_2 + NI(s) \rightarrow CO_2(s)$	$1.000 \times 10^{-05\dagger}$	0.0	0.00
6.	$CO + NI(s) \rightarrow CO(s)$	$5.000 \times 10^{-01\dagger}$	0.0	0.00
7.	$H(s) + H(s) \rightarrow NI(s) + NI(s) + H_2$	$2.545 \times 10^{+19}$	0.0	81.21
8.	$O(s) + O(s) \rightarrow NI(s) + NI(s) + O_2$	$4.283 \times 10^{+23}$	0.0	474.95
9.	$CH_4(s) \rightarrow CH_4 + NI(s)$	$8.705 \times 10^{+15}$	0.0	37.55
10.	$H_2O(s) \rightarrow H_2O + NI(s)$	$3.732 \times 10^{+12}$	0.0	60.79
11.	$CO_2(s) \rightarrow CO_2 + NI(s)$	$6.447 \times 10^{+07}$	0.0	25.98
12.	$CO(s) \rightarrow CO + NI(s)$	$3.563 \times 10^{+11}$	0.0	111.27
	$\theta_{CO(s)}$			$-50.00^\ddagger$
13.	$H(s) + O(s) \rightarrow OH(s) + NI(s)$	$5.000 \times 10^{+22}$	0.0	97.90
14.	$OH(s) + NI(s) \rightarrow H(s) + O(s)$	$1.781 \times 10^{+21}$	0.0	36.09
15.	$H(s) + OH(s) \rightarrow H_2O(s) + NI(s)$	$3.000 \times 10^{+20}$	0.0	42.70
16.	$H_2O(s) + NI(s) \rightarrow H(s) + OH(s)$	$2.271 \times 10^{+21}$	0.0	91.76
17.	$OH(s) + OH(s) \rightarrow H_2O(s) + O(s)$	$3.000 \times 10^{+21}$	0.0	100.00
18.	$H_2O(s) + O(s) \rightarrow OH(s) + OH(s)$	$6.373 \times 10^{+23}$	0.0	210.86
19.	$C(s) + O(s) \rightarrow CO(s) + NI(s)$	$5.200 \times 10^{+23}$	0.0	148.10
20.	$CO(s) + NI(s) \rightarrow C(s) + O(s)$	$1.354 \times 10^{+22}$	-3.0	116.12
	$\theta_{CO(s)}$			$-50.0^\ddagger$
21.	$CO(s) + O(s) \rightarrow CO_2(s) + NI(s)$	$2.000 \times 10^{+19}$	0.0	123.60
	$\theta_{CO(s)}$			$-50.00^\ddagger$
22.	$CO_2(s) + NI(s) \rightarrow CO(s) + O(s)$	$4.653 \times 10^{+23}$	-1.0	89.32
23.	$HCO(s) + NI(s) \rightarrow CO(s) + H(s)$	$3.700 \times 10^{+21}$	0.0	0.00
	$\theta_{CO(s)}$			$50.00^\ddagger$
24.	$CO(s) + H(s) \rightarrow HCO(s) + NI(s)$	$4.019 \times 10^{+20}$	-1.0	132.23
25.	$HCO(s) + NI(s) \rightarrow CH(s) + O(s)$	$3.700 \times 10^{+24}$	-3.0	95.80
26.	$CH(s) + O(s) \rightarrow HCO(s) + NI(s)$	$4.604 \times 10^{+20}$	0.0	109.97
27.	$CH_4(s) + NI(s) \rightarrow CH_3(s) + H(s)$	$3.700 \times 10^{+21}$	0.0	57.70
28.	$CH_3(s) + H(s) \rightarrow CH_4(s) + NI(s)$	$6.034 \times 10^{+21}$	0.0	61.58
29.	$CH_3(s) + NI(s) \rightarrow CH_2(s) + H(s)$	$3.700 \times 10^{+24}$	0.0	100.00
30.	$CH_2(s) + H(s) \rightarrow CH_3(s) + NI(s)$	$1.293 \times 10^{+22}$	0.0	55.33
31.	$CH_2(s) + NI(s) \rightarrow CH(s) + H(s)$	$3.700 \times 10^{+24}$	0.0	97.10
32.	$CH(s) + H(s) \rightarrow CH_2(s) + NI(s)$	$4.089 \times 10^{+24}$	0.0	79.18
33.	$CH(s) + NI(s) \rightarrow C(s) + H(s)$	$3.700 \times 10^{+21}$	0.0	18.80
34.	$C(s) + H(s) \rightarrow CH(s) + NI(s)$	$4.562 \times 10^{+22}$	0.0	161.11
35.	$CH_4(s) + O(s) \rightarrow CH_3(s) + OH(s)$	$1.700 \times 10^{+24}$	0.0	88.30
36.	$CH_3(s) + OH(s) \rightarrow CH_4(s) + O(s)$	$9.876 \times 10^{+22}$	0.0	30.37
37.	$CH_3(s) + O(s) \rightarrow CH_2(s) + OH(s)$	$3.700 \times 10^{+24}$	0.0	130.10
38.	$CH_2(s) + OH(s) \rightarrow CH_3(s) + O(s)$	$4.607 \times 10^{+21}$	0.0	23.62
39.	$CH_2(s) + O(s) \rightarrow CH(s) + OH(s)$	$3.700 \times 10^{+24}$	0.0	126.80
40.	$CH(s) + OH(s) \rightarrow CH_2(s) + O(s)$	$1.457 \times 10^{+23}$	0.0	47.07
41.	$CH(s) + O(s) \rightarrow C(s) + OH(s)$	$3.700 \times 10^{+21}$	0.0	48.10
42.	$C(s) + OH(s) \rightarrow CH(s) + O(s)$	$1.625 \times 10^{+21}$	0.0	128.61

* Arrhenius parameters for the rate constant written in the form: $k = AT^\beta \exp(-E/RT)$;
† Sticking coefficient; ‡ Coverage dependent activation energy; Total surface site density is $\Gamma = 2.6 \times 10^{-9}$ mol/cm^2; More details and download on www.detchem.com

5. Modeling mass and heat transport

The general conservation equation for the transport of chemical species can be described as

$$\frac{\partial(\rho Y_k)}{\partial t} = -\nabla \cdot \left(\rho \vec{u} Y_k + \vec{J}_k\right) + \dot{\omega}_k, +\dot{s}_k. \tag{48}$$

Here, Y_k is the mass fraction of species k, ρ is the mixture density, $\vec{u}$ is the velocity vector, $\dot{\omega}_k$ is the rate of production/consumption of any chemical species in the channels as a result of gas-phase reactions, $\dot{s}_k$ is the production/consumption of the species k as a result of surface reactions, and $\vec{J}_k$ is the diffusive mass flux of species k. The surface reaction rate, $\dot{s}_k$, is given by Eq. (47), Eq. (35) or by any other rate formulation. The gas-phase species source term $\dot{\omega}_k$ shall be neglected here. For flow through channels, J_k, is defined by

$$\vec{J}_k = \vec{j}_k + \vec{j}_k{}', \tag{49}$$

where

$$\vec{j}_k = -\rho \mathcal{D}_{km} \nabla Y_k, \quad \text{and} \quad \vec{j}_k{}' = -Y_k \sum_{k=1}^{K_g} \vec{j}_k \tag{50}$$

such that

$$\sum_{k=1}^{K_g} \vec{J}_k = 0. \tag{51}$$

The diffusive mass flux, $\vec{J}_k$, can also be evaluated using the generalized Stefan–Maxwell equations, which automatically guarantees the condition of the net flux to be zero [74–76].

In the case of porous electrodes the situation becomes more complex due to Knudsen diffusion. The multi-component species transport in porous media can be well represented by the Dusty Gas Model (DGM). The DGM can be written as an implicit relationship among molar concentrations, fluxes, concentration gradients, and a pressure gradient as

$$\sum_{l \neq k} \frac{[X_l]J_k - [X_k]J_l}{[X_{\text{tot}}]\mathcal{D}_{kl}^{\text{e}}} + \frac{J_k}{\mathcal{D}_{k,kn}^{\text{e}}} = -\nabla[X_k] - \frac{B_g[X_k]}{\mu \mathcal{D}_{k,kn}^{\text{e}}} \nabla p. \tag{52}$$

Equation (52) can be used to develop a direct formulation of the diffusive molar flux vector [65]:

$$\vec{J}_k = -\left[\sum_{l=1}^{K_g} \mathcal{D}_{kl}^{\text{DGM}} \nabla[X_l] + \left(\sum_{l=1}^{K_g} \frac{\mathcal{D}_{kl}^{\text{DGM}}[X_l]}{\mathcal{D}_{l,kn}^{e}} \right) \frac{B_g}{\mu} \nabla p \right]. \tag{53}$$
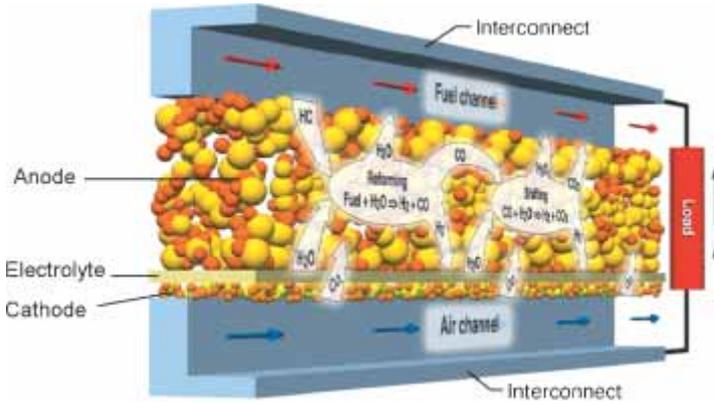
Fig. 2. A schematic presentation of a cut-away view of a planar, anode-supported SOFC unit in co-flow configuration operated with hydrocarbon containing fuels; adapted from Zhu *et al.* [65].

The first term on the right hand side of Eq. (53) represents the diffusive and the second one the viscous flux. $\mathcal{D}_{kl}^{\mathrm{DGM}}$ are defined as DGM diffusion coefficients given as [65]

$$\mathcal{D}_{kl}^{\mathrm{DGM}} = \mathcal{H}^{-1} , \tag{54}$$

where the elements of the $\mathcal{H}$ matrix are

$$h_{kl} = \left[\frac{1}{\mathcal{D}_{k,kn}^{\mathrm{e}}} + \sum_{j \neq k} \frac{X_j}{\mathcal{D}_{kj}^{\mathrm{e}}} \right] \delta_{kl} + (\delta_{kl} - 1) \frac{X_k}{\mathcal{D}_{kl}^{\mathrm{e}}} . \tag{55}$$

The effective binary diffusivity $\mathcal{D}_{kl}^{\mathrm{e}}$ is given by

$$\mathcal{D}_{kl}^{\mathrm{e}} = \frac{\epsilon}{\tau} \mathcal{D}_{kl} , \tag{56}$$

where $\mathcal{D}_{kl}$ is the binary diffusivity, ϵ and τ are the porosity and tortuosity, respectively, of the porous media. The permeability of the porous media B_g in Eq. (53) is given by Kozeny–Carman relationship [77]:

$$B_g = \frac{\epsilon^3 d_p^2}{72\tau(1-\epsilon)^2} . \tag{57}$$

The effective Knudsen diffusion coefficient appearing in Eq. (53) is given by

$$\mathcal{D}_{k,kn}^{\mathrm{e}} = \frac{4}{3} \frac{\epsilon}{\tau} r_{\mathrm{p}} \sqrt{\frac{8RT}{\pi W_k}} . \tag{58}$$

Instead of using the complex DGM equation to calculate the species mass flux, sometimes a simpler modified Fickian approach may be appropriate as well. According to this method the species mass flux J_k is defined as

$$J_k = -\rho \mathcal{D}_{k,\mathrm{eff}} \nabla Y_k \,, \tag{59}$$

where $\mathcal{D}_{k,\mathrm{eff}}$ is defined as

$$\frac{1}{\mathcal{D}_{k,\mathrm{eff}}} = \frac{1}{\mathcal{D}_{km}^{\mathrm{e}}} + \frac{1}{\mathcal{D}_{k,\mathrm{kn}}^{\mathrm{e}}} \,. \tag{60}$$

Here, the effective Knudsen diffusion coefficient, $\mathcal{D}_{k,\mathrm{kn}}^{\mathrm{e}}$, is defined by Eq. (58), and the effective mixture diffusion coefficient is given by

$$\mathcal{D}_{km}^{\mathrm{e}} = \frac{\epsilon}{\tau} \mathcal{D}_{km} \,. \tag{61}$$

The velocity and pressure fields can be resolved by solving the equation of continuity

$$\frac{\partial \rho}{\partial t} + \nabla \cdot (\rho \vec{u}) = \mathcal{S}_{\mathrm{m}} \tag{62}$$

and momentum

$$\frac{\partial (\rho \vec{u})}{\partial t} + \nabla \cdot (\rho \vec{u} \vec{u}) = -\nabla p - \frac{2}{3} \nabla \cdot (\mu \nabla u) + \nabla \cdot \left[\mu \left(\nabla \vec{u} + \nabla \vec{u}^{\mathrm{T}} \right) \right] + \vec{F} \,. \tag{63}$$

Here, μ is the mixture viscosity, p is the pressure, and $\vec{F}$ is any external force acting on the system.

The temperature field within a SOFC stack can be described by

$$\frac{\partial (\rho C_p T)}{\partial t} + \nabla \cdot (\rho \vec{u} C_p T) = \nabla \cdot (k \nabla T) - \sum_{k=1}^{K_g} h_k \vec{J}_k + Q \,. \tag{64}$$

Here, C_p is the specific heat capacity of the species mixture/material under consideration, k is the thermal conductivity of species mixture/material, h_k is the specific enthalpy of species k, and Q represents any volumetric heat source. When Eq. (64) is solved for solid regions, the second term on the right side vanishes, and the second term on the left side represents convective energy transfer due to rotational or translational motion of the solids. Furthermore, while solving the energy equation for electrodes, the thermal conductivity k must be approximated by the effective conductivity. The heat source, Q, may include heat release due to chemical and electrochemical reactions, Ohmic resistance etc.

Since the cell charging time is very short compared to other phenomena occurring in the cell, the potential field in the stack/cell, ϕ, can be solved using the steady state relationship:

$$\nabla^2 \phi = \begin{cases} -\frac{i}{\sigma} & \text{at TPB} \\ 0 & \text{elsewhere .} \end{cases} \tag{65}$$

Here, i is the current density obtained from the Butler–Volmer equation (Eq. (1), or Eqs. (21) and (28)), and σ is the conductivity of the respective component under consideration, which is given by Eq. (11) for the electrolyte.

6. Modeling SOFC unit cells and stacks

The coupled interactions of physics and chemistry occurring in SOFCs are extremely complex and some of the phenomena are fairly unknown. Models of the physical and chemical processes in the SOFC, therefore, are usually simplified representations of the actual physics and chemistry, and accuracy of the model predictions can not be guaranteed unless the model has been validated using experimental observations obtained for a wide range of operating conditions. Numerical simulation of the behavior of SOFCs based on detailed models of the various complex physical and chemistry processes and their interactions is therefore a recently started new field in fuel cell research.

A SOFC stack is the core component of a complete SOFC system, which also includes pre-reformer, fuel ejector, after burner, pre-heater etc. All these components are equally important and have to be considered for the prediction of the efficiency and performance of a SOFC power generation system. This article is limited to modeling SOFC unit cells and stacks.

A schematic presentation of a SOFC monolithic stack for counter flow configuration is shown in Fig. 3. A single channel out of the stack for a co-flow configuration is depicted in Fig. 2. Here the fuel species are transported from the fuel channel through the porous anode towards the TPB, and the products formed by the electrochemical charge transfer reaction at the TPB are transported back towards the fuel channel. If hydrocarbons such as natural gas are used as primary fuel, in most cases, the fuel is pre-reformed to a certain extent (often completely) prior to feeding to the fuel cell stack. Nevertheless, the anode of the cell also provides ample opportunity for the fuel to undergo reforming. The reforming reactions produce synthesis gas, H_2 and CO, undergoing charge transfer reactions at the TPBs. The reaction products (H_2O and CO_2) further replenish the reforming chemistry within the cell. However, the reaction products also dilute the fuel thereby decreasing the Nernst potential as well as the current density. Generally the reactants and the products have opposite fluxes within the porous anode. For example, H_2 always has a flux towards the TPB, while the product H_2O always has a flux away from the TPB. Furthermore the diffusion limitation within the porous electrodes can lead to
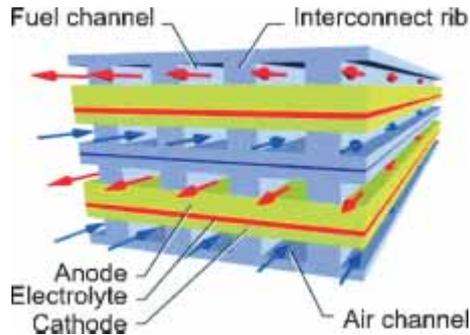
Fig. 3. A three-dimensional schematic presentation of counter flow SOFC stack (Courtesy of R. J. Kee, Colorado School of Mines.)

steep gradients of the species concentration profiles at the electrode–channel interfaces.

The electrochemistry model equations described in Sect. 3 represent an internal boundary condition for the stack simulation. These equations have to be coupled with models for the fluid flow in the fuel and air channels, the transport of the chemical species in the electrodes, the thermo chemical kinetics in the anode (for any fuel other than pure hydrogen), mass and heat transport in the fuel/air channels and electrodes, and heat transport in the entire solid structure.

6.1 Three-dimensional models

The equations discussed above represent a general description of physical and chemical processes occurring in a SOFC cell/stack. These equations can be used to simulate the transient or steady-state behavior of the SOFC cell/stack with appropriate boundary conditions. In most studies with three-dimensional (3d) stack simulations, commercial CFD codes combined with custom built routines for electrochemistry are used. Three dimensional models are highly useful for the computation of the temperature distribution within the cell/stack. For instance, a 3d model can account for the heat transfer to/from all the three interconnect walls that surrounds the fuel and air channels, while a two-dimensional model accounts only for heat transfer to the top wall. In general, the MEA extends beyond the breadth of the fuel and air channels, and electrochemical reactions can proceed in the extended region due to gas diffusion. This effect can be studied in three-dimensional models only.

Keegen *et al.* [78] carried out a transient 3d thermo-fluid analysis of start-up of a single stack using the commercial CFD code STAR-CD [79]. The computational grid of 470 000 cells and the resulting temperature distribution within the stack, which is operated with hydrogen and air, are shown in Figs. 4
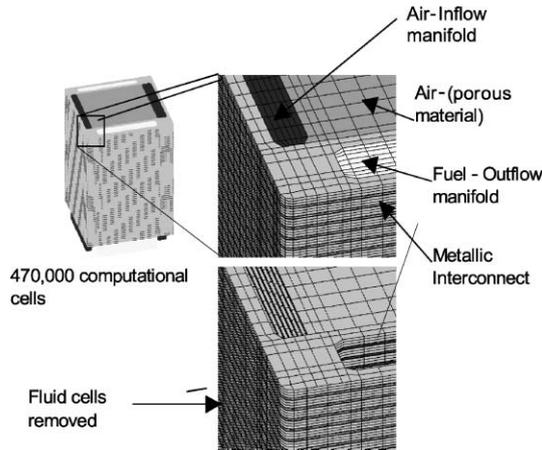
Fig. 4. Thermal-fluids stack computational model geometry of Keegan *et al.* [78].
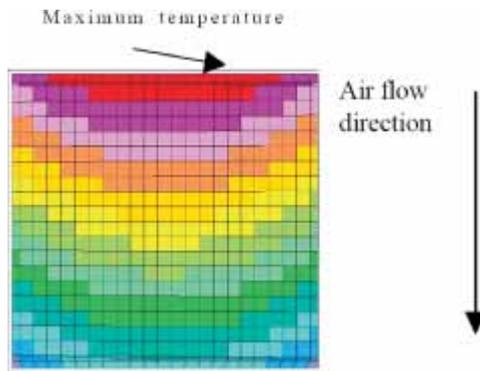

Fig. 5. Predicted cell temperature contours from 600 to 800 °C in the transient 3d CFD simulation of Keegan *et al.* [78] at 25 min after start-up.

and 5, respectively. The individual cells are simulated by a porous media model for the active area. Figure 5 reveals significant temperature gradients within the cell.

The same group [80] studied the temperature, current density, and flow distribution within anode and cathode of a cross-flow, counter-flow, and co-flow stack using a 3d model geometry and applying cyclic boundary conditions. For a given average cell temperature, similar fuel utilizations were found for all flow configurations. For a cross-flow configuration, the operation with a partially reformed gasoline consisting of 36% H_2, 35% CO, 5% H_2O, 5% CO_2, and 19% N_2 at 0.7 V resulted in maximum temperature gradients, while the co-flow configuration showed the smallest temperature gradient.

6.2 Two-dimensional models

Two-dimensional (2d) models are generally used for unit cell simulations. A schematic presentation of a co-flow planar unit cell is shown in Fig. 2. The draw backs of 2d simulations compared to 3d simulations are discussed in the previous section. However, 2d models are fast in computation due to the possible geometry reductions as explained in [56]. In case of tubular cells center symmetry usually is assumed. Li *et al.* [81] reported the modeling of a tubular SOFC running on pre-reformed methane fuel using axi-symmetric geometry and compared the results with experimental observations. By fixing the operating cell potential their model spatially resolves a number of local properties such as electro motoric force (EMF), current density, temperature, and species concentrations. Their study also reveals the effect of fuel and oxygen depletion on local EMF; both EMF and local current density peak near the fuel inlet due to the high fuel availability and decrease further downstream. Xue *et al.* [82] also reported the application of quasi 2d model for modeling of a tubular SOFC unit cell.

In case of planar cell modeling, a 2d section is considered as representative of the entire cell operation. A quasi 2d model for planar unit cell was recently presented by Zhu *et al.* [65], taking into account direct internal reforming. The model assumed plug flow in the channels, and the porous media transport was modeled using DGM. The local current density at the TPB, the composition of all species in the fuel channel and in the porous anode are computed for a given cell voltage as shown in Fig. 6 for isothermal conditions. The model proposed can also take into account gas-phase reactions. Since a detailed surface reaction mechanism is integrated into the numerical simulation, the surface coverages inside the anode are also predicted. Figure 6 reveals the strong gradients in species concentrations along the 5 cm long flow channel and also the gradients perpendicular to it inside the 1 mm thick anode for the conditions indicated in the caption of Fig. 6.

Recently, this quasi-two dimensional model [65] was extended to predict the temperature distribution in a single planer cell operated with humidified methane (97% CH_4 and 3% H_2O) as fuel [83]. The interconnect walls were assumed to be adiabatic. Assuming H_2 as the only electrochemically active species, the local variation of temperature in the fuel and air channels as well as in the interconnects are shown in Fig. 7. At the entrance, the fuel stream looses heat to the comparatively cold air entering the air channel, hence the temperature of the air stream increases. As reforming starts, the temperature of the fuel stream further drops and now, the temperature of the air stream as well. However, further downstream, the temperature begins to increase as a result of exothermic thermo catalytic cell reactions such as water-gas shift, electrochemical oxidation as well as Ohmic and activation losses. There is no significant temperature difference between the anode side interconnect and the fuel channel in contrast to the behavior at the cathode side interconnect/air channel.
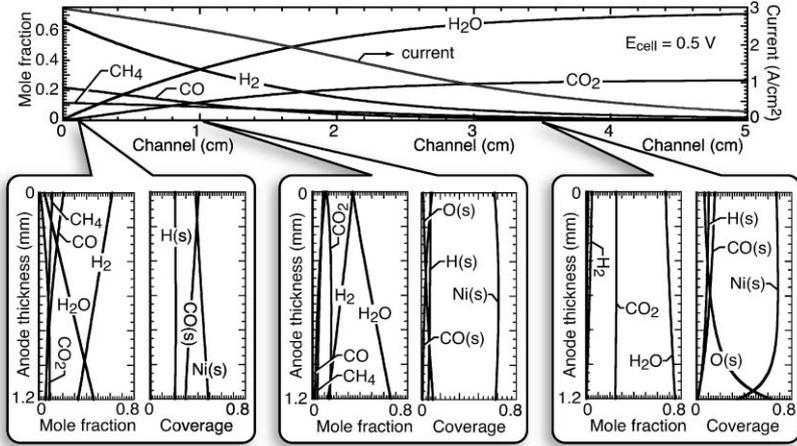
Fig. 6. Application of a 2d model for numerical prediction of the profiles in fuel channel and anode taken from Zhu *et al.* [65]; inlet fuel composition is 66% H_2, 22% CO, and 12% CH_4; isothermal condition (800 °C). The upper panel shows gas-phase mole fractions as a function of distance along the 5 cm channel. The lower panels show gas-phase mole fractions and surface coverages through the thickness of the porous anode at three positions along the channel. The upper boundary of the drop-down panels is at the anode-channel interface and the lower boundary is at the anode–electrolyte interface.

Interestingly, the temperature of the anode side interconnect is lower than that of the fuel channel, while the cathode side interconnect has a higher temperature than the air channel, which is primarily caused by thermal radiation from the cathode electrode to the interconnect. Current density and reversible potential for the cell operated at 0.7 V are shown in Fig. 8. The reversible potential peaks near the inlet due to the low temperature. For H_2 electrochemical oxidation, the typical drop of the reversible potential with increasing temperature and fuel dilution is revealed. After the short increase near the cell inlet, the current density then drops due to reforming reactions (lower temperature), and increases again further downstream due to the increased temperature.

This 2d model approach was also used to study the influence of air flow rate, anode thickness, catalyst loading, and pre-reforming on the performance of a planar anode-supported cell, which was 10 cm in length and operated with 40% CH_4 and 60% H_2O as fuel at 0.7 V. Since the cell voltage was fixed, fuel utilization is the most significant parameter for cell efficiency. For any particular operating condition, an optimal anode thickness exists for efficiency and power density (Fig. 9); maxima were achieved for an anode thickness of approximately 0.5 mm under the conditions of this study. In the case of direct internal fuel reforming, the anode serves as catalyst for the production of H_2 and CO that further participate in the charge transfer reactions at the three-phase boundary. In the case of thin anodes, the smaller amount
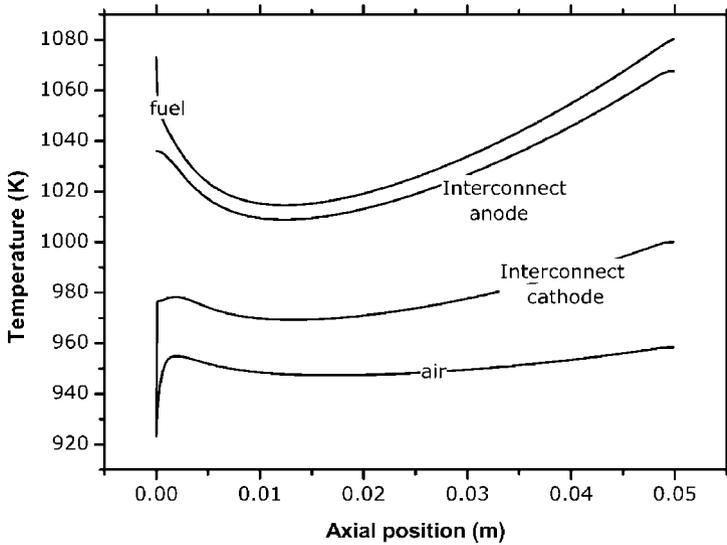
Fig. 7. Application of a 2d model for numerical predictions of temperature profiles within the flow channels as well as in the interconnects in a cell operated with humidified methane as fuel [83]. The inlet fuel and air streams are at 800 °C and 650 °C, respectively; operating cell potential is 0.7 V.
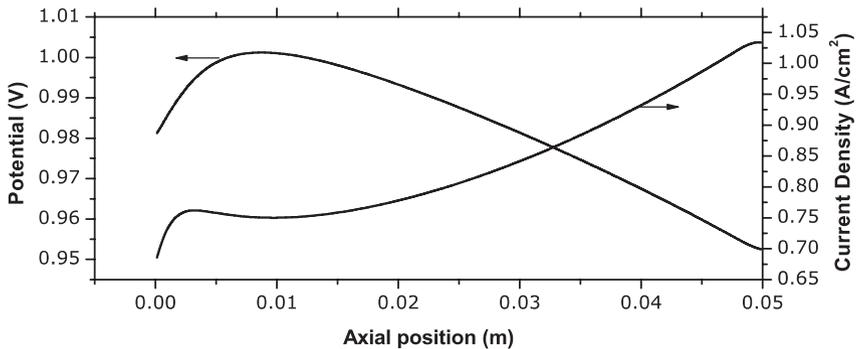

Fig. 8. Application of a 2d model for numerical predictions of current density and reversible potential of a cell operated with humidified methane as fuel [83]. The inlet fuel and air streams are at 800 °C and 650 °C, respectively; operating cell potential is 0.7 V.

of catalyst limits the amount of H_2 produced leading to lower average current density, efficiency, and power density. For thick anodes, the H_2 and CO production by the (endothermic) fuel reforming is increased, however, on the costs of a larger temperature drop close to channel inlet resulting in decreased performance.
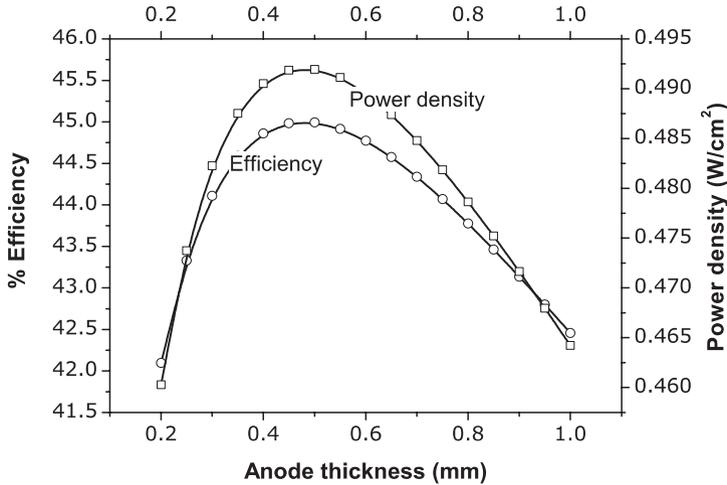
Fig. 9. Application of a 2d model for numerical predictions of the effect of anode thickness on efficiency and power density for a cell operated under adiabatic conditions. The inlet fuel consists of 40% CH_4 and 60% H_2O at 800 °C. Cathode inlet is assumed to be air at 650 °C.

6.3 One-dimensional models

A one-dimensional model treats the entire unit cell as a plug flow reactor model and simplifies the model equations representing the physics and chemistry occurring in the cell. For example, a 2d model does not need to account for the concentration losses within electrodes, because it spatially resolves the species concentration profiles in the porous electrode (Fig. 6) and, hence, provides the local species concentration at the TPB needed for the electrochemistry model. In contrast to that, in the one-dimensional model, the concentration losses have to be calculated explicitly. In two consecutive publications, Aguiar *et al.* [57, 84] reported the steady state and dynamic operation of a planar anode supported cell with pre-reformed methane fuel. Figure 10 shows their predicted current density, voltage, and overpotential losses along the flow direction in the cell [57]. In this case, the inlet fuel was a simulated mixture resulting from 10% pre-reforming of a fuel having a steam to carbon (S/C) ratio of 2, and the cathode feed was assumed to be air, both entering at 800 °C. The cell geometry consisted of 500 μm anode and interconnect, 50 μm cathode, and 20 μm electrolyte.

Compared to fully elliptic 2d and 3d models, one dimensional models are computationally much less time consuming with the compromise of loosing the details of flow field, temperature, and species distributions. Furthermore it is not possible for one dimensional models to resolve the electric field within the cell.
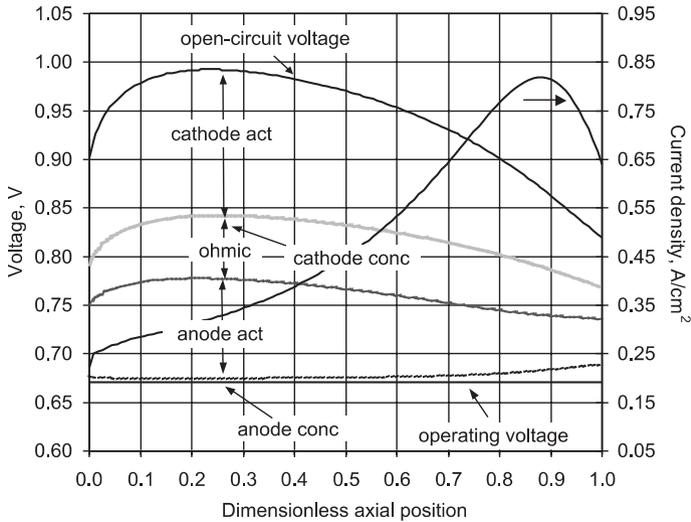
Fig. 10. Predicted voltage, current density, and contribution of various potential losses along the cell length for a fuel utilization of 95%. Fuel inlet consists of a species mixture resulting from 10% pre-reformed fuel with a steam to carbon ratio of two; taken from Aguiara *et al.* [57].

6.4 Zero-dimensional models

Zero dimensional models, also known as box models, are the simplest ones used to analyze the electrochemical performance of the cell. These models solve only the electrochemistry model equations described in Sect. 3. For an anode supported cell, the concentration polarization is shown in Fig. 11; the calculation is based on Eqs. (12) and (13).

In many cases, parameters such as exchange current density, reaction order dependence of exchange current density, tortuosity, and porosity are unknown. Under these circumstances zero dimensional models can be used to deduce electrochemical model parameters from button cell experimental data and these parameters can be used to model and predict the performance of other cell configurations as described in Zhu *et al.* [65]. However one has to make sure that the parameters deduced by fitting zero dimensional models are physically realistic.

7. Summary and conclusion

Solid-Oxide Fuel Cells are potential candidates for high efficiency energy conversion. The physico-chemical processes that occur in a SOFC are extremely complex and interdependent. Therefore, any modeling effort should account for the coupled interactions of mass and heat transport, thermo-catalytic chem-
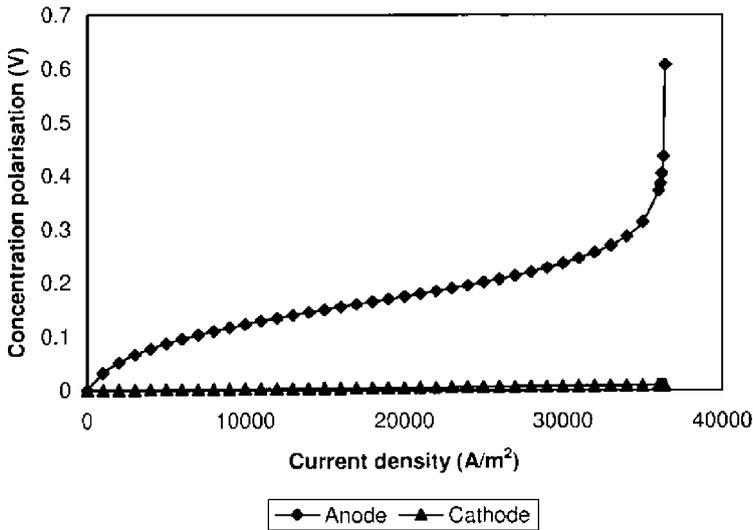
Fig. 11. Anodic and cathodic concentration overpotential; reproduced from Chan *et al.* [54].

istry, and electrochemistry. More sophisticated models may also account for the electric field generated in the cell.

This article lined out the general background of the components of a state-of-the-art SOFC unit cell and principles of electrochemistry, heterogeneous chemistry, and mass and heat transport to present modeling approaches. The general equations discussed can be simplified to represent 2d or 1d models. Results from the literature were presented to demonstrate the capability of numerical models in predicting local distributions of species concentrations, temperature, and current density.

Zero-dimensional electrochemical model equations form the core of SOFC numerical models. Furthermore zero-dimensional model equations alone can be used to interpret button cell experimental observations and deduce electro-chemical model parameters, which can be further used in the modeling of unit cells of a stack. 1d models are highly efficient in predicting the general behavior of the unit cell, provided that appropriate boundary conditions and model parameters are used. A more detailed and accurate description of local distribution of flow field, temperature, species concentrations, current density, and potential losses can be obtained by the use of 2d models. 3d models are generally used for stack simulation to predict the temperature distribution and the resulting thermal stresses within the stack as a result of varying coefficients of thermal expansion (CET) of the various cell components.

The direct use of hydrocarbons and alcohols as fuels, one of the advantages of SOFCs, leads to thermo-catalytic chemistry in the anode (direct internal re-

forming) with the consequence of a complex composition of the gas phase at the anode–electrolyte TPB and hence effects on the electrochemistry. Here in particular, understanding of the elementary processes and the development of reliable models and computational tools for the simulation of the SOFC behavior are challenging tasks, but are expected to accelerate optimization of SOFC designs and applications.

Acknowledgement

Notations

A	Pre-exponential factor (mol, m, s)
B_g	Permeability (m)
C_p	Specific heat capacity ($J\,kg^{-1}\,K^{-1}$)
d_p	Particle/pore diameter (m)
D	Diffusivity ($m^2\,s^{-1}$)
E_a	Activation energy ($J\,mol^{-1}$)
E^0	Electro motoric force, EMF (V)
E_{rev}	Nernst potential, OCV (V)
E_{cell}	Cell voltage/potential (V)
F	Faraday number ($C\,mol^{-1}$)
$\vec{F}$	External force ($kg\,m^{-2}\,s^{-2}$)
h	Specific enthalpy ($J\,kg^{-1}$)
i	Current density ($A\,m^{-2}$)
i_0	Exchange current density ($A\,m^{-2}$)
J_k	Species flux ($mol\,m^{-2}\,s^{-1}$)
k	Rate constant (mol, m, s)
k	Thermal conductivity ($J\,m^{-1}\,s^{-1}\,K^{-1}$)
K_g	Number of gas-phase species
K_r	Number of reactions
K_s	Number of surface species
l	Length/Thickness (m)
n_e	Number of electrons transferred (-)
p	Pressure (Pa)
Q	Volumetric heat source ($J\,m^{-3}\,s^{-1}$)
R	Gas constant ($J\,mol^{-1}\,K^{-1}$)
R	Electric resistance ($V\,A^{-1}$)
r	Reaction rate (kg, mol, s)
r_p	Pore radius (m)

S_m Mass source term (kg m^{-3} s^{-1})

$\dot{s}$ Molar production rate (surface reactions) (mol m^{-2} s^{-1}), (mol m^{-3} s^{-1})

t time (s)

T Temperature (K)

$\vec{u}$ Velocity (m s^{-1})

W_k Molecular weight of k'th species (kg mol^{-1})

$[X]$ Concentration (mol m^{-3})

X Mole fraction

Y Mass fraction

Greek symbols

α asymmetry factor/charge transfer coefficient for global kinetics ($-$)

β asymmetry factor/charge transfer coefficient for elementary step kinetics ($-$)

Γ Surface site density (mol m^{-2})

γ_0 Sticking coefficient ($-$)

ϵ Porosity

η Overpotential (V)

μ Viscosity (kg m^{-1} s^{-1})

ν Net stoichiometric coefficient ($-$)

ν' Stoichiometric coefficient of reactant ($-$)

ρ Density (kg m^{-3})

σ Conductivity (S m^{-1})

θ Surface coverage ($-$)

τ Tortuosity ($-$)

$\dot{\omega}$ Molar production rate (gas phase reactions) (mol m^{-3} s^{-1})

Superscripts

des   desorption

Subscripts

a   anode

act   activation

c   cathode

conc   concentration

e   electrolyte

k species index

ohm   Ohmic

rev   reversible

tot   total

Abbrevations

CFD	Computational Fluid Dynamics
DGM	Dusty Gas Model
OCV	open circuit voltage/potential
PEMFC	Proton Exchange Membrane Fuel Cell
SOFC	Solid-Oxide Fuel Cell
TPB	Three phase boundary
YSZ	yttria stabilized zirconia

References

1. J. Larminie and A. Dicks, *Fuel Cell Systems Explained*. 2nd edn., John Wiley and Sons Ltd, West Sussex, England (2003).
2. K. A. Adamson, A. Baker, and D. Jollie, *Opening doors to fuel cell commercialisation: Fuel cell systems: A survey of world wide activity*. Technical Report, Fuel cell today (2004).
3. A. Weber and E. Ivers-Tiffée, J. Power Sources **127** (2004) 273.
4. Y. Matsuzaki and I. Yasuda, Solid State Ionics **152**–**153** (2002) 463.
5. A. Bieberle, *The Electrochemistry of Solid Oxide Fuel Cell Anodes: Experiments, Modeling, and Simulations*. Ph.D. Thesis, Swiss Federal Institute of Technology (2000).
6. EG&G Services Parsons, Inc. Science Applications International Corporation. Fuel Cell Handbook, 5th edn. (2000).
7. R. N. Basu, G. Blass, H. P. Buchkremer, D. Stver, F. Tietz, E. Wessel, and I. C. Vinke, J. European Ceramic. Soc. **25** (2005) 463.
8. P. Charpentier, P. Fragnauda, D. Schleicha, and E. Gehainb, Solid State Ionics **135** (2000) 373.
9. J. R. Wilson, W. Kobsiriphat, R. Mendoza, H. Y. Chen, J. M. Hiller, D. J. Miller, K. Thornton, P. W. Voorhees, S. B. Adler, and S. A. Barnett, Nature materials **5** (2006) 541.
10. J. H. Koh, Y. S. Yoo, J. W. Park, and H. C. Lim, Solid State Ionics **149** (2002) 157.
11. B. A. Boukamp, Nature materials **2** (2003) 294.
12. S. Tao and J. T. Irvine, Nature materials **2** (2003) 320.
13. S. McIntosh, H. He, S. Lee, O. C. Nunes, V. V. Krishnan, J. M. Vohs, and R. J. Gorte, J. Electrochem. Soc. **151** (2004) A604.
14. S. Lee, J. M. Vohs, and R. J. Gorte, J. Electrochem. Soc. **151** (2004) A1319.
15. E. P. Murray, T. Tsai, and S. A. Barnett, Nature **400** (1999) 649.
16. N. Nagakawa, H. Sagara, and K. Kato, J. Power Sources **92** (2001) 88.
17. W. Zhu and S. Deevi. Materials Sci. Eng. A **362** (2003) 228.
18. A. C. Co, S. J. Xia, and V. I. Birss, J. Electrochem. Soc. **152** (2005) A570.
19. E. Maguire, B. Gharbage, F. Marquesb, and J. Labrinchab, Solid State Ionics **127** (2000) 329.
20. H. Tu and U. Stimming, J. Power Sources **127** (2004) 284.
21. T. Tsai and S. A. Barnett, Solid State Ionics **93** (1997) 207.
22. M. Juhl, S. Primdahl, C. Manon, and M. Mogensen, J. Power Sources **61** (1996) 173.
23. R. Williford and P. Singh, J. Power Sources **128** (2004) 45.
24. P. Holtappels and C. Bagger, J. European Cerm. Soc. **22** (2002) 41.

25. S. Jiang, J. Power Sources **124** (2003) 390.
26. S. P. S. Badwal, R. Deller, K. Foger, Y. Ramprakash, and J. P. Zhang, Solid State Ionics **99** (1997) 297.
27. W. Zhu and S. Deevi, Mat. Research Bulletin **38** (2003) 957.
28. T. Ishihara and N. M. S. abd O. Yamamoto, *High Temperature Solid Oxide Fuel Cells Fundamentals, Design and Applications*. Elsvier, Amsterdam, The Netherlands (2003).
29. W. Zhu and S. Deevi, Mat. Sci. Eng. A **348** (2003) 227.
30. J. W. Fergus, Mat. Sci. Eng. A **397** (2005) 271.
31. L. Jian, P. Jian, X. Guangyuanb, W. Shunxu, and X. Jianzhong, J. Power Sources **157** (2006) 368.
32. J. W. Fergus, Solid State Ionics **171** (2004) 1.
33. Z. Zeng and K. Natesan, Solid State Ionics **167** (2004) 9.
34. A. Atkinson, S. Barnett, R. J. Gorte, J. T. S. Irvine, A. J. Mcevoy, M. Mogensen, S. C. Sighal, and J. Vohs, Nature **3** (2004) 17.
35. J. Liu and S. A. Barnett, Solid State Ionics **158** (2003) 11.
36. Y. Lin, Z. Zhan, J. Liu, and S. A. Barnett, Solid State Ionics **176** (2005) 1827.
37. Z. Zhan and S. A. Barnett, Science **308** (2005) 844.
38. B. C. H. Steele, Nature **400** (1999) 619.
39. N. M. Sammes, R. J. Boersma, and G. A. Tompsett, Solid State Ionics **135** (2000) 487.
40. T. Hibino, A. Hashimoto, K. Asano, M. Yano, M. Suzuki, and M. Sano, Electrochem. Solid State Lett. **5** (2002) A242.
41. Z. Shao, S. M. Haile, J. Ahn, P. D. Ronney, Z. Zhan, and S. A. Barnett, Nature **435** (2005) 795.
42. R. M. Ormerod, *High Temperature Solid Oxide Fuel Cells Fundamentals Design and Applications*. Elsevier (2003).
43. B. Feng, C. Y. Wang, and B. Zhu, Electrochem. Solid State Lett. **9** (2006) A80.
44. Z. Cheng, S. Zha, L. Aguilar, and D. Wand, Electrochem. Solid State Lett. **9** (2006) A31.
45. G. O. Lauvstad, R. Tunold, and S. Sunde, J. Electrochem. Soc. **149** (2002) E497.
46. Y. Matsuzaki and I. Yasuda, J. Electrochem. Soc. **147** (2000) 1630.
47. S. P. Jiang and S. P. S. Badwal, J. Electrochem. Soc. **144** (1997) 3777.
48. E. A. Liese and R. S. Gemmen, J. Eng. Gas Turb. Power **127** (2005) 86.
49. K. Kendall, Nature **404** (2000) 233.
50. C. M. Finnerty, N. J. Coe, R. H. Cunningham, and R. M. Ormerod, Catalysis Today **46** (1998) 137.
51. B. C. H. Steele and A. Heinzel, Nature **414** (2001) 345.
52. H. Zhu and R. J. Kee, J. Power Sources **117** (2003) 61.
53. V. M. Janardhanan and O. Deutschmann, J. Power Sources **162** (2006) 1192.
54. S. Chan, K. Khor, and Z. Xia, J. Power Sources **93** (2000) 130.
55. T. L. Nguyen, T. Honda, T. Kato, Y. Iimura, K. Kato, A. Negishi, K. Nozaki, M. Shiono, A. Kobayashi, K. Hosoda, Z. Cai, and M. Dokiya, J. Electrochem. Soc. **151** (2004) A1230.
56. R. Bove and S. Ubertini, J. Power Sources **159** (2006) 543.
57. P. Aguiara, C. Adjimana, and N. Brandona, J. Power Sources **138** (2004) 120.
58. A. M. Sukeshini, B. Habibzadeh, B. P. Becker, C. A. Stoltz, B. W. Eichhorn, and G. S. Jackson, J. Electrochem. Soc. **153** (2006) A705.
59. J. Mizusaki, H. Tagawa, T. Saito, T. Yamamura, K. Kamitani, K. Hirano, S. Ehara, T. Takagi, T. Hikita, M. Ippommatsu, S. Nakagawa, and K. Hashimoto, Solid State Ionics **70–71** (1994) 52.
60. P. Holtappels, I. C. Vinke, L. G. J. de Haart, and U. Stimming, J. Electrochem. Soc. **146** (1999) 2976.

61. B. de Boer, *SOFC Anode: Hydrogen Oxidation at Porous Nickel and Nickel/Yttria Stabilized Zirconia Cermet Electrodes*. Ph.D. Thesis, University of Twente, The Netherlands (1998).
62. M. Vogler, W. G. Bessler, J. Warnatz, A. Bieberle, and L. J. Gauckler, In: 7th European SOFC Forum. Lucerne, Switzerland (2006).
63. W. G. Bessler, J. Warnatz, and D. G. Goodwin, Solid State Ionics **177** (2007) 3371.
64. A. Bieberle, L. P. Meier, and L. J. Gauckler, J. Electrochem. Soc. **148** (2001) A646.
65. H. Zhu, R. J. Kee, V. M. Janardhanan, O. Deutschmann, and D. G. Goodwin, J. Electrochem. Soc. **152** (2005) A2427.
66. P. Costamagna, A. Selimovic, M. D. Borghi, and G. Agnew, Chem. Engg. Journal **102** (2004) 61.
67. A. J. Bard and L. R. Faulkner, *Electrochemical Methods Fundamentals and Applications*. John Wiley & Sons, Inc (2001).
68. G. K. Gupta, A. M. Dean, E. S. Hecht, H. Zhu, and R. J. Kee, In: *Solid Oxide Fuel Cells IX (SOFC-IX)*. S. C. Singhal and J. Mizusaki (Eds.), Vol. 1, pp. 6679–688 (2005).
69. A. L. Dicks, K. D. Pointon, and A. Siddle, J. Power Sources **86** (2000) 523.
70. M. Boudart, AIChE J. **18** (1972) 465.
71. J. Xu and G. F. Froment, American Institute of Chemical Engineers **35** (1989) 88.
72. K. Ahmed and K. Foger, Catalysis Today, American Institute of Chemical Engineers **63** (2000) 479.
73. E. S. Hecht, G. K. Gupta, H. Zh, A. M. Dean, R. J. Kee, L. Maier, and O. Deutschmann, Appl. Catal. A. General **295** (2005) 40.
74. R. B. Bird, W. E. Stewart, and E. N. Lightfoot, *Transport Phenomena*. 1st edn., John Wiley & Sons (1960).
75. R. J. Kee, M. E. Coltrin, and P. Glarborg, *Chemically Reacting Flow*. John Wiley & Sons, Inc. (2003).
76. Fluent Inc., Lebanon, NH 03766. Fluent user manual 6.1, www.fluent.com.
77. J. Baer, *Dynamics of Fluids in Porous Media*. American Elsevier, New York (1972).
78. K. Keegan, M. Khaleel, L. Chick, K. Recknagle, S. Simner, and J. Deibler, *Analysis of a Planar Solid Oxide Fuel Cell Based Automotive Auxiliary Power Unit*. Technical Report, SAE, 2002-01-0413 (2002).
79. Computational Dynamics Ltd. STAR-CD Version 3.05 Methodology (1998).
80. K. P. Recknagle, R. E. Williford, L. A. Chick, D. R. Rector, and M. A. Khaleel, J. Power Sources **113** (2003) 109.
81. P. W. Li, L. Schaefer, and M. K. Chyu, J. Heat Transfer **126** (2004) 219.
82. X. Xue, J. Tang, N. Sammes, and Y. Du, J. Power Sources **142** (2005) 211.
83. V. M. Janardhanan and O. Deutschmann, Chem. Eng. Sci. (2007) doi:10.1016/j.ces. 2007.01.043
84. P. Aguiar, C. Adjiman, and N. Brandon, J. Power Sources **147** (2005) 136.